Annals of 3D Printed Medicine 19 (2025) 100212

Contents lists available at ScienceDirect

Annals of 3D Printed Medicine

journal homepage: www.elsevier.com/locate/stlm

Research paper

Conversion of an FDM printer to direct ink write 3D bioprinter utilizing an efficient and cost-effective extrusion system

Y. H. Dang, Elise Dauzat, Asif Istiak, Kevin Jackson, Victoria Songe, Luke West, Md Imrul Kayes, Md Saiful Islam, Tanvir R. Faisal *

Department of Mechanical Engineering, University of Louisiana at Lafayette, Lafayette, LA 70503, USA

ARTICLE INFO

Keywords:
Bioprinter
Converted 3D printer
Peristaltic pump
Hydrogel
Bioink

ABSTRACT

3D bioprinting has emerged as a transformative technology in biomedical engineering, enabling the fabrication of functional tissues through the precise deposition of cell-laden biomaterials. However, the widespread adoption of this technology is constrained by the prohibitive costs of commercial bioprinting systems. We present a cost-effective solution through the conversion of an open-source fused deposition modeling (FDM) 3D printer into a direct ink write bioprinter by integrating a peristaltic pump-based extrusion system. The modified dual-extruder system demonstrates successful deposition of hydrogel-based bioinks across varying viscosities, producing well-defined scaffold architectures. The printer's open-source control architecture facilitates retraction capabilities, high-speed movements, and customizable printing parameters, enhancing operational flexibility. This development represents a significant step toward democratizing low-cost bioprinting technology, making it accessible to academic institutions and research facilities with limited resources.

1. Introduction

In recent years, extrusion-based deposition of hydrogel-based bioink has become a widely used method for producing 3D biostructures with tailored geometry [1] and controlled microstructures [2]. This technique involves cell-laden or cell-free bioinks composed of synthetic or natural materials, or a combination of both. 3D bioprinting has gained significance in the medical field and biomedical research due to its accessibility and emerging applications such as tissue scaffolds, organs-on-a-chip, regenerative medicine, and drug delivery systems [3,4]. However, the research and development of 3D bioprinters are still ongoing to overcome various challenges, including customization difficulties, limited compatibility of bioinks, dependence on fixed printing software and hardware systems, and high costs. The high price point of 3D bioprinters often requires dedicated funds, which can limit even well-funded research activities and core operations.

Based on different principles and requirements [5], the printing system has been modified in 3D printing process to be used for various purposes including: (a) direct ink writing (DIW) [6], (b) selective laser sintering (SLS) [7], (c) fused deposition modeling (FDM) [8,9], (d) fiber fabrication [10] (e) stereolithography (SLA) [11], and (f) digital light processing (DLP) [12]. Several approaches and conversions have been occurring to provide open-source and well-developed bioprinters with specific research targets. The DIW printer is a low-cost, high precision printer [13] where the ink material is continuously extruded from the nozzle by mechanical or pneumatic pressure, and a specific pattern is produced on the substrate according to the set program. The FDM printer is a type of additive manufacturing technology that builds objects layer by layer using thermoplastic materials. Converting an FDM printer to a DIW printer involves several modifications and additions to adapting the machine for bioprinting or other applications requiring the precise continuous deposition of various viscous ink materials through the nozzle under controlled extrusion force. However, a number of efforts have continued to convert an FDM 3D printer into a bioprinter even though the conversion process is challenging.

One example is the freeform reversible embedding of suspended hydrogels (FRESH) technology, which uses a syringe-based extruder to print in a support bath environment [14–16]. Joshua et al. [17] customized the 3D FDM printer by changing the motion control board. To release the bioink from the extruder, researchers used techniques [5] including UV-DIW [18], embedded multimaterial extrusion bioprinting [19], and microgel print bedding [20], which have individual adverse effects on printing live cells. Blaeser et al. [21] demonstrated the use of multiple extruders with compressed air assembly to print multi-layered

* Corresponding author at: 241 E Lewis St, Mechanical Engineering, University of Louisiana at Lafayette, LA, 70503, USA.
E-mail address: tanvir.faisal@louisiana.edu (T.R. Faisal).

https://doi.org/10.1016/j.stlm.2025.100212
Received 18 December 2024; Received in revised form 23 May 2025; Accepted 28 May 2025
Available online 6 June 2025

objects. Mechanical pressure on the piston of the syringe by motorized sliding guide [22], stepper motor [23], assembly of stepper motor and linear actuator [24] are popular customizations to control the extrusion process, but these methods often fail to guarantee air bubble-free printed objects due to irregular mechanically pressurized bubbles in the nozzle. Wijnen et al. [25] and Loannidis et al. [13] provided a solution with an open-source pump system in the syringe to build a 3D bioprinter. Furthermore, the extrusion process is often limited because of bioink's viscosity. Kyle et al. [26] listed significant research that highlighted the effort to change hydrogels to avoid the issue of different viscosities. Yan et al. [27] altered the pump system to extrude bioinks with different viscosities. Although the recently developed 3D bioprinters can print bio-implants and bio-materials, the diameter of the needle affects the extrusion of bioinks due to shear stress, which affects the resolution of printed objects [28]. Small nozzle diameters lead to higher shear stress and cell damage, while clogging is a limitation of small-diameter needles [29]. Straight nozzles and small outlet diameters require higher pressures and impose higher shear stresses on cells during extrusion, but they can increase printing resolution [30]. Discontinuities may develop in the deposited bioink if the printing speed is higher than the extrusion rate, whereas the ink may spread and overflow if the print speed is below the extrusion rate [31]. In addition, shear stress is a critical factor in extrusion-based bioprinting that significantly impacts cell viability especially for a cell-laden biomaterial (bioink). High shear stress can damage cell membranes and cytoskeletons, leading to cell death, and even if cells survive, excessive shear stress can negatively impact their function (e.g., differentiation, proliferation) [32,33].

Considering the multitude of challenges in bioprinting, including precise extrusion control and accommodating a wide range of bioink viscosities, our primary objective was to develop a simplified adaptation of a 3D FDM printer's mechanical components to address these requirements. Our research established a methodological framework demonstrating that commercial 3D printers can be effectively and economically transformed into bioprinters. In this work, we focused on converting the extrusion component and process through the integration of a syringe and peristaltic pump system, enabling high-fidelity bioprinting with bioinks that can be used for tissue engineering. The other objective of this work was the performance evaluation of the converted bioprinter computationally via finite element modeling and by comparing the geometric measurements of the printed scaffolds with that of the CAD models.

2. Materials and methods

2.1. Hardware

A conventional 3D FDM printer was selected as the base platform due to its cost-effectiveness and wide availability. The printer features a temperature-controlled printing bed capable of reaching and maintaining 60 °C in the printing chamber, which facilitates the curing of deposited biomaterials. Printing speed can be precisely controlled through open-source software. The selected 3D printer incorporates an automatic dual extrusion system capable of printing filaments at temperatures up to 240 °C. The built-in extruder was augmented with a pump and syringe-based extrusion system, enabling the dispensing of hydrogels with a varying mixing ratio. Fig. 1 shows the schematic of the conversion of a 3D FDM printer into an extrusion-based bioprinter following the proposed strategy.

2.1.1. Extruder block

An extruder block was designed to accommodate the new pump and syringe system, while utilizing the printer's dual extrusion capability. The dimensional parameters of the extruder block were carefully engineered to ensure proper limit switch activation. The design incorporated mounting points to securely fasten to the metal block, with concentric alignment of their respective extrusion holes (Fig. 2). To prevent materials leakage at their interface between the extruder and the metal blocks, the extrusion holes in the metal block were threaded to accommodate quick-disconnect fittings, while a continuous hose runs through the peristaltic pump, the extrusion block, and into the quick-disconnect fitting.

The extruder block features a two-piece design to facilitate easy assembly and maintenance. Four corner holes were machined to accommodate nuts and bolts to secure the two pieces together. The block incorporates 0.55-inch (13 mm) diameter channels designed to provide direct support and guidance for the tubing. With overall dimensions of 2 inches (50 mm) in depth and 3.5 inches (88 mm) in width, the block effectively engages (contacts) with the printer's synchronization touch points. The design features two distinct sections (Fig. 2)—a brown portion with a height of 2 inches (50 mm) and a grey portion measuring 1.85 inches (48 mm) in height. This intentional dimensional offset ensures proper alignment with the printer's existing mounting configuration. Both components were fabricated using PLA filament through 3D printing.

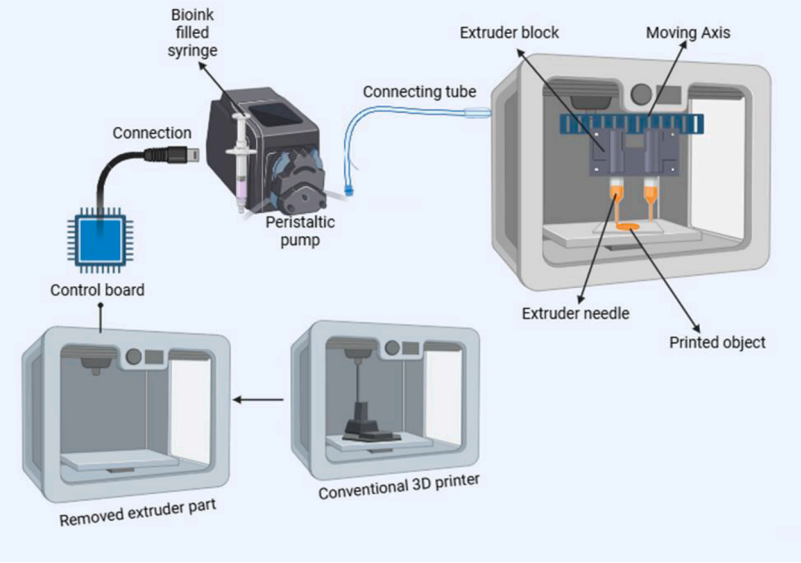

Fig. 1. A schematic of the conversion of a 3D FDM printer into an extrusion-based bioprinter.

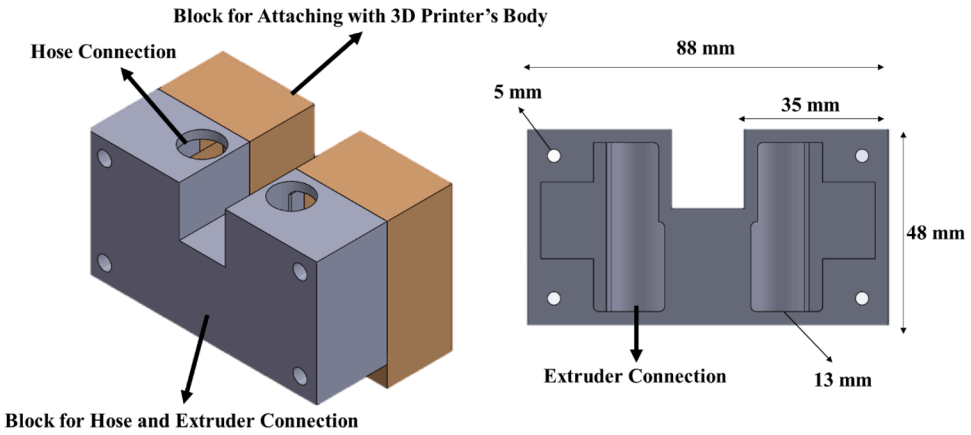

Fig. 2. A 3D model of the extruder block (left) and its sectional view (right).

2.1.2. Peristatic pump with static motor

The system incorporates dual Kamoer peristaltic pumps (Fig. 3) to provide actuation pressure to develop a pressure-driven extrusion system, enabling the handling of materials with viscosities ranging from 1 kPa-s to several kPa-s. This pump was selected based on its commercial availability, ease of implementation, and capability to transfer both low and high-viscosity liquids. Each pump was coupled with a NEMA17 stepper motor, matching the specifications of the printer's original extruder (stepper) motors. The motor operates at a maximum voltage of 24 V and current of 1.2 A, achieving rotational speeds up to 350 rpm with flow rates between 20–110 ml/min. The motors maintain operational stability within a temperature range from 0 to 40 °C.

2.1.3. Connective tube

In this bioprinter, we utilized PharMed BPT tubing—a polypropylene-based thermoplastic elastomer (TPE) with an inner diameter of 3.2 mm and outer diameter of 6.4 mm (type S/B16). This tubing supports flow rates up to 110 ml/min and was directly connected to the extruding block and nozzle (Fig. 3). The tube material maintains operational stability across a temperature range of −51 to 132 °C. While the tubing's expected service life exceeds 1000 h, this duration increases inversely with pump head speed. The PharMed BPT material demonstrates high resistance to chemical exposure and ultraviolet radiation, providing effective protection for sensitive bioinks.

2.1.4. Syringe extruder

A syringe-based extrusion system was implemented to facilitate the dispensing of hydrogels and liquids across varying viscosities (Fig. 4). The system utilizes syringes with an inner diameter of 20 mm, each connected to a pump and fitted with a luer lock needle. The inlet configuration, shown in Fig. 4, depicts a bioink-filled syringe attached to the left side of the pump. The bioprinter incorporated a dual-syringe setup with two luer lock needles, enabling both simultaneous and accelerated printing capabilities.

The needles were secured in the extruder position using integrated plastic screws. The inner diameter of the steel nozzle (needle) was 0.40 mm, and the length of the needle was 5 mm. The complete needle assembly installation within the extruder position is illustrated in Fig. 4.

2.2. Design files summary

The extruder system comprises two 3D-printed blocks designed to accommodate the bioink delivery hose. The CAD models were designed in SolidWorks 2024, and the drawings are available in the repositories mentioned in Table 2 of the supplementary file. The printer's slicing software processes the G-code files for bioprinting.

2.3. Bill of materials

A comprehensive list of components and materials used in the device construction, including their costs, is provided in Table 3 of the supplementary materials. While most components are readily available through Amazon or local markets, the pump's specific online procurement source is exclusively listed in the table.

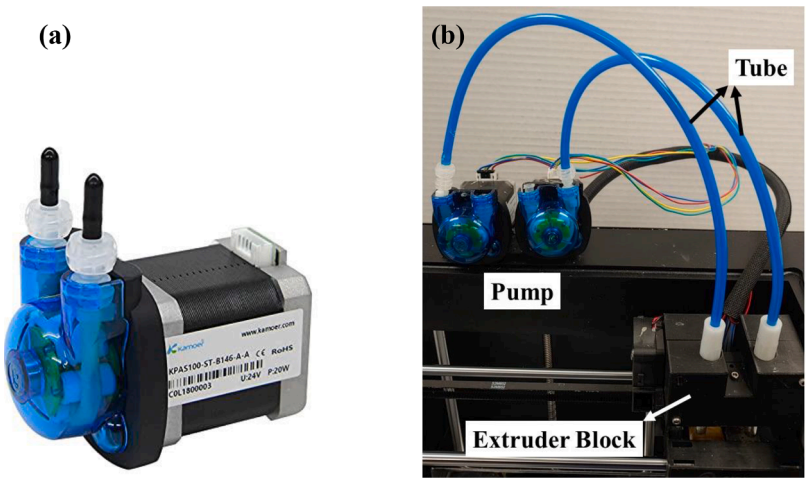

Fig. 3. **(a)** Kamoer peristaltic pump and stepper motor assembly and **(b)** B16 tube used to connect the pump and extruder block in the converted bioprinter.

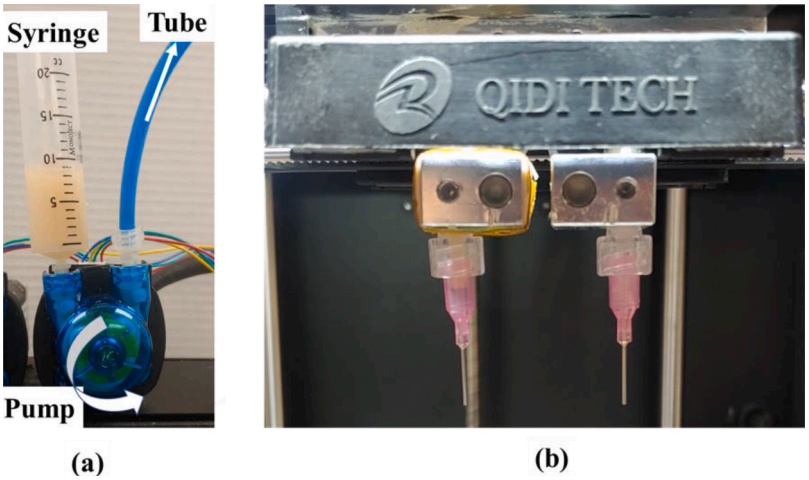

Fig. 4. **(a)** Syringe installed in a pump inlet, and **(b)** Installed luer lock needle.

2.4. Assembly instructions

The conversion process begins with connecting the printer's controller board wire to the pump's motor, which is then mounted on the printer's upper frame using double-sided adhesive tape. The tubing is installed within the pump's cylindrical blades, designed to facilitate bioink transfer through counterclockwise rotation. The tube's distal end is secured through the extruder block's aperture using a supporting nozzle. The extruder assembly incorporates screwed needle caps for needle mounting. As a printing bed, we used an upside-down Petri dish with a height of 40.4 mm. Fig. 5 illustrates the complete setup of the converted bioprinter. The Petri dish, inverted and measuring 40.4 mm in height, serves as the printing substrate. Fig. 5 presents the fully assembled bioprinter configuration.

2.5. Operation instructions

2.5.1. Scaffold design for printing

The test scaffold for evaluating the printing performance was designed in Autodesk Fusion 360 CAD software and exported in STL file format. Fig. 6 shows the dimensions of the designed scaffold with a uniform edge thickness of 0.2 mm. This specific simplified square grid model was considered to evaluate the precision of the printer and integrity of the bioink. Grid-like structures were chosen to clearly demonstrate the accuracy of printing resolution.

2.5.2. Bioink fabrication

A standardized hydrogel-based bioink fabrication process, suitable for 3D-printed cartilage scaffolds, was implemented in this study. The bioink formulation comprised sodium alginate, chitosan, deionized water, and collagen in varying ratios to simulate cartilage-like tissue properties [34]. Multiple mixing ratios were evaluated to assess printing outcome variability. Collagen was incorporated to enhance the bioink's mechanical properties, specifically stiffness and strength. Bioink B was selected as the primary formulation for collagen incorporation due to its superior viscosity, strength, and printing characteristics [34]. All the chemicals were purchased from Sigma Aldrich and used without further purification. Component masses were measured using a digital mass comparator. The powder components were vigorously mixed in water, followed by thermal curing at 50 °C for 1 h in an oven. The mixture was subsequently cooled to an ambient temperature and stored at 3–5 °C. Prior to printing, the bioink was equilibrated to room temperature for 45 min. The compositional ratios of various bioink formulations are shown in Table 1.

2.5.3. 3D bioprinting

For printing, the bioink-filled syringe is required to be installed in the left chamber of the peristaltic pump, and the other (right) chamber is connected to the pipe, which is consequently attached to the extruder block (Fig. 5). The STL file is needed to slice in the slicer software where Z-offset height can be adjusted according to the height of petri dish so

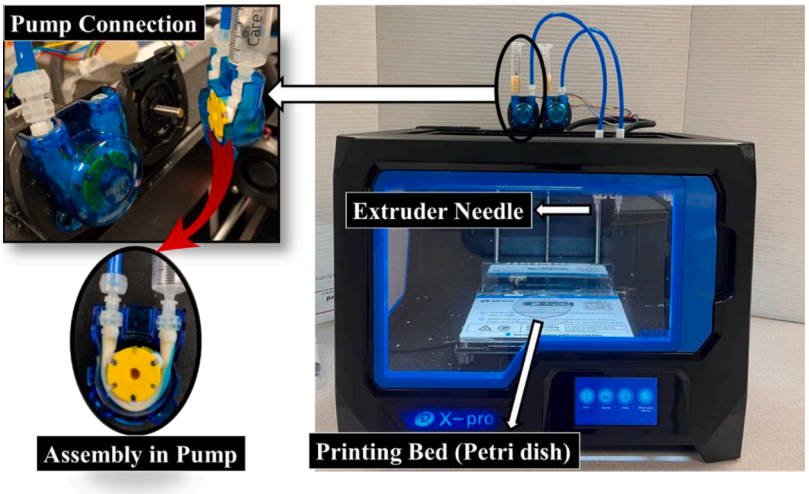

Fig. 5. A complete assembly of the converted bioprinter.

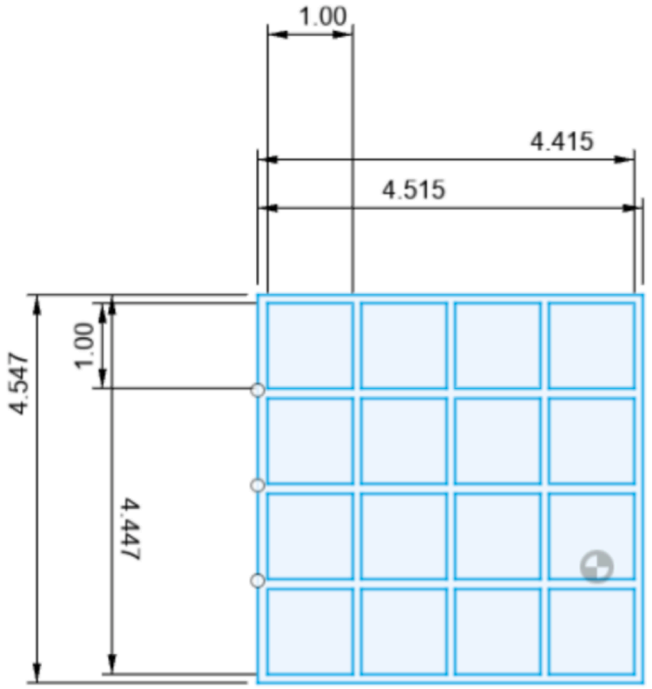

Fig. 6. CAD design of the scaffold with dimensions in cm.

Table 1
Weight compositions of constituents for different bioinks.

Bioink	Alginate (g)	Chitosan (g)	Collagen (g)	Water (ml)
A	2	1	0	20
B	2	1.5	0	20
C	2	2	0	20
D	2	1.5	1	20
E	2	1.5	1.5	20

that the distance between extruder and bed can be kept at 0.20 mm to maintain the target 0.2 mm thickness of the grid. During the fabrication process, the printing parameters such as temperature, flow rate, and print speed can be flexibly changed similar to conventional printing. For printing with the in-house made viscous bioinks, we set the extruder and bed temperature at 25 °C.

The modular nature of the additional assembly allows for seamless integration with the printer while maintaining conventional printer functionality. System validation focused on evaluating printed object quality to verify the accuracy and precision of the bioprinting system. Printing parameters and software settings were only optimized for single-layer object production.

The cleaning protocol encompasses both the bioink transfer hose within the pump and the connecting hose between the pump and extruder, facilitating thorough cleaning before and after printing or when switching between bioink types. Fig. 7(a) demonstrates the cleaning procedure for the pump-installed tube, while Fig. 7(b) shows the water-based cleaning method for connecting tubes. Prior to printing, the connecting tubes underwent bioink priming.

2.5.4. Computaional fluid dynamics analysis

Computational fluid dynamics (CFD) analysis was conducted based on the simulated flow to calculate the shear stress distribution within the bioink, particularly along the needle walls and at the needle outlet. For CFD analysis, a simplified 2D geometric model of the tube and needle was developed in Solidworks 2024 to replicate the configuration of a peristaltic pump. The tube was modeled with an inner diameter of 3.2 mm and a length of 138 mm, featuring two localized compression zones

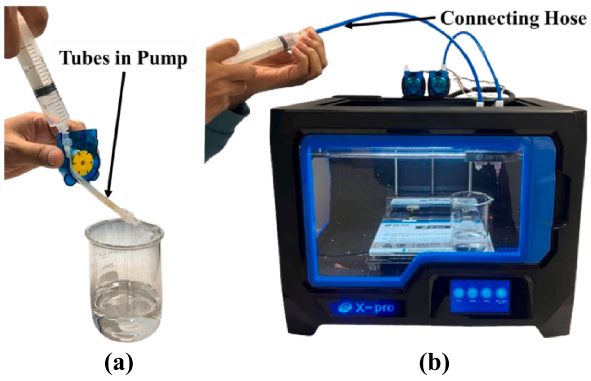

Fig. 7. Cleaning procedure of the connector tubes of the bioprinter: (a) cleaning of pump-installed tube, and (b) water-based cleaning of connecting tubes.

representing the pump's roller-induced deformation. A needle with a diameter of 0.4 mm and a length of 5 mm was positioned at the tube's outlet. For CFD analysis, the CAD model was imported into Ansys Fluent (2021 R2), and appropriate material properties were assigned. The inlet velocity was derived from the G-code corresponding to the printing of the test grid.

Since Bioink D demonstrated the most consistent and well-defined printed structures, its rheological properties were used in the CFD analyses. The viscosity profile of Bioink D, spanning a shear rate range of 0.1 to 1000 s^{-1}, was experimentally determined using a modular compact rheometer (Anton Paar). The bioink was modeled as a non-Newtonian, laminar, and viscous-dominated flow under peristaltic motion within the defined geometry. 2D, unsteady, and incompressible Navier–Stokes equations governing mass and momentum conservation [35] was employed in this CFD analysis. The following differential equation is the mass balance equation:

$$\left[\frac{\partial u}{\partial x}+\frac{\partial v}{\partial y}\right]=0 \tag{1}$$

X-direction momentum conservation

$$\rho\left[\frac{\partial u}{\partial t}+u\frac{\partial u}{\partial x}+v\frac{\partial u}{\partial y}\right]=\rho F_x-\frac{\partial p}{\partial x}+\mu\left[\frac{\partial^2 u}{\partial x^2}+\frac{\partial^2 u}{\partial y^2}\right] \tag{2}$$

Y-direction momentum conservation

$$\rho\left[\frac{\partial v}{\partial t}+u\frac{\partial v}{\partial x}+v\frac{\partial v}{\partial y}\right]=\rho F_y-\frac{\partial p}{\partial y}+\mu\left[\frac{\partial^2 v}{\partial x^2}+\frac{\partial^2 v}{\partial y^2}\right] \tag{3}$$

where p denotes static pressure, ρ is fluid density, μ is dynamic viscosity, and t is for time. u, v are the velocities and F_x, *and* F_y are the body forces in the x, *and* y coordinate directions, respectively.

A no-slip boundary condition was applied to the stationary tube wall, while the top and bottom ends of the tube were fully constrained along both coordinate axes. For fluid flow, boundary conditions at the inlet and outlet were defined such that the total stress was assumed to be zero. The computational mesh was generated using the default meshing settings in Ansys Fluent.

3. Results

Analysis of the printed structures revealed minimal dimensional deviation from the target thickness of 0.20 mm along the grid lines, though greater variation was observed at intersection points. The grid patterns demonstrated consistent bioink distribution along the printed lines, with post-printing deviations attributed to variations in bioink viscosity. Crosslinking treatments proved essential for maintaining structural integrity of the extruded patterns. In this study, we considered

physical crosslinking mechanisms via the process of freeze-thaw. This process helps the polymer chains to entangle and form a gel-like structure due to the formation of ice crystals within the solution, thereby locking the components together. This method is often used to create porous scaffolds for tissue engineering applications [36,37]. Quantitative analysis of pattern deviation was performed using ImageJ software.

Fig. 8 displays the printing outcomes achieved using 5 distinct bioink formulations. Each bioink demonstrated unique printing characteristics. Bioink A exhibited non uniform material distribution during printing, with significant spreading attributed to its low viscosity. Bioinks B and C maintained consistent line widths throughout the grid structure, though both demonstrated material dispersion at intersection points due to chitosan-induced swelling. Bioink D achieved optimal printing resolution, attributed to its balanced collagen content. In contrast, Bioink E produced discontinuous printing lines, a limitation associated with its elevated collagen concentration.

The side-view (height) of the printed scaffolds, shown in the Fig. S1 (supplementary file), demonstrates dimensional consistency with the top-view presented in Fig. 8. The height of scaffolds was approximately 0.1 mm. Fig. 9 illustrates the dimensional deviations between the printed structures and their corresponding CAD designs. Specifically, Fig. 9(a) quantifies the percentage deviation in line width, while Fig. 9 (b) presents the variations in joint thickness at grid intersections. Although the extrusion system accurately followed the G-code-defined paths, the printed structures exhibited dimensional variations correlating with bioink viscosity. Notable deviations were observed with Bioink A, which demonstrated considerable line-width variation due to excessive material spreading.

Bioinks B and C exhibited dispersed printing patterns, resulting in mean line-width deviations of 10 % and 6 %, respectively. In contrast, Bioinks D and E demonstrated superior dimensional control with overall deviations of approximately 5 % or less, with Bioink D achieving optimal dimensional fidelity (mean deviation of 3 %). Analysis of joint thickness (Fig. 9b) revealed that Bioink A produced near-nominal thickness (line width) values (0.25–0.26 mm), albeit with high variability. Bioinks B, C, and D showed consistent but moderately elevated joint thicknesses ranging from 0.28–0.32 mm. These results demonstrate the significant influence of the bioinks' rheological properties on extrusion characteristics through the selected nozzle, even with precise positional control from the bioprinting system.

Surface irregularities in the Petri dish substrate can significantly impact printing quality, potentially causing either extrusion interruptions or excessive material deposition, resulting in discontinuous patterns. Fig. 10 illustrates these printing disruptions and their characteristic manifestations. Additional printing discontinuities may arise from non-homogeneous bioink formulations. The converted printer demonstrates potential for multi-layer fabrication capabilities comparable to conventional 3D printers while utilizing rapid-curing bioink formulations. A detailed video demonstration of the printing process is provided in the supplementary materials.

The converted system demonstrated dual-printing capability, enabling the fabrication of single scaffolds using multiple bioink formulations. Fig. 11 illustrates a multi-layer structure produced through dual-extrusion printing utilizing distinct bioinks. The first layer was deposited using Bioink B through an 18-gauge needle, followed by Bioink D deposition through a 20-gauge needle, the latter selected for its demonstrated lower dispersion characteristics in single-nozzle printing trials.

The contour plot presented in Fig. 12 illustrates the shear stress distribution along the tube and attached nozzle (needle). The highest shear stress (0.65 bar) was observed, but at the needle wall, approaching approximately 0.47 bar, and the shear stress dropped to 0.2 bar in the middle of the needle. The shear stress within the wall of the tube remained around 0.008 bar but dropped further at the center of the tube. However, a noticeable increase was detected in regions of geometric constriction, 0.04 bar and 0.08 bar in the first and second compressed zones, respectively. Supplementary Fig. S2 provides additional detail, highlighting localized elevations in shear stress at various points along the tube and nozzle.

4. Discussion

We successfully demonstrated the conversion of a commercial 3D FDM printer into a low-cost 3D bioprinter capable of accommodating diverse bioink viscosities. The system was optimized through iterative parameter refinement to achieve precise printing outcomes. The modified extrusion mechanism effectively delivers bioinks through exit needles while preventing air entrapment, demonstrating compatibility with various mixing ratios and producing accurate representations of targeted anatomical structures. Furthermore, the conversion maintains the original printer's software and hardware architecture, requiring minimal modifications while incorporating dual-gate extrusion capability

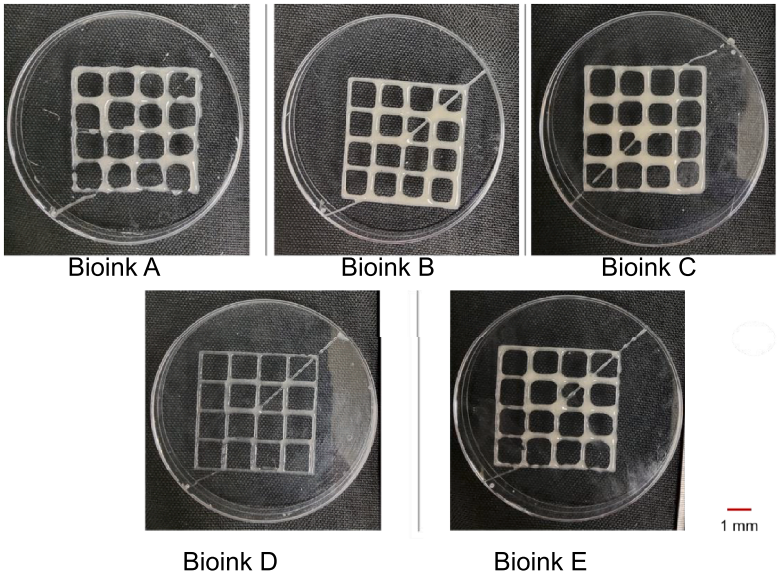

Fig. 8. Examples of square-grid printed scaffolds with five different Bioinks A, B, C, D, and E.

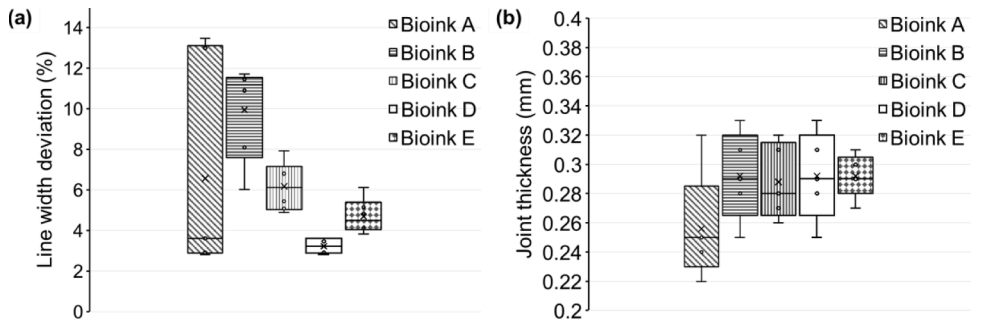

Fig. 9. (a) Deviation of grid line width and (b) joint thickness of different printed scaffolds with Bioinks A, B, C, D, and E.

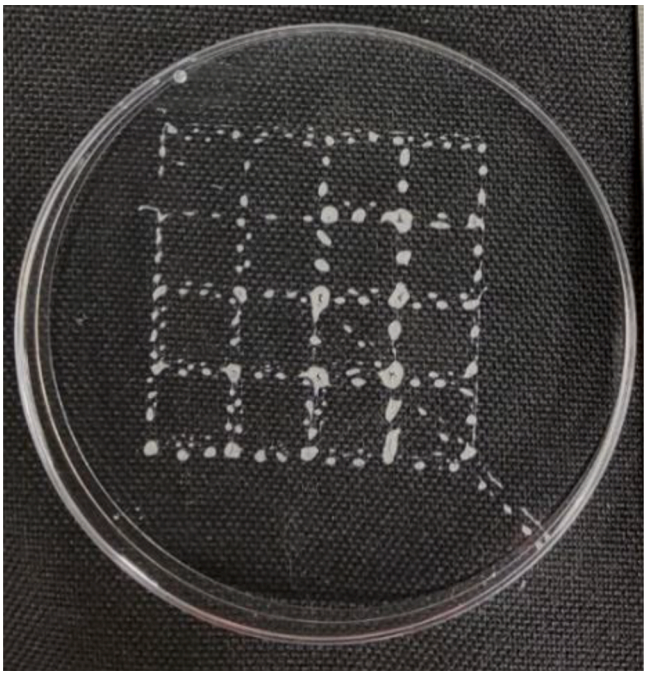

Fig. 10. An example of disruptive printed scaffold.

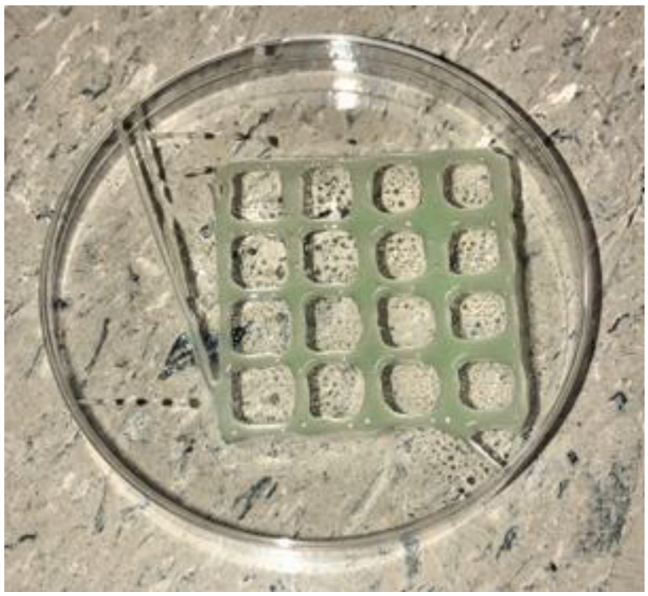

Fig. 11. A multilayer printed scaffold using two different bioinks (Bioinks B and D) extruded from two syringe-based extruders.

with optimized needle diameters for precise multi-material printing. The system demonstrates high-fidelity reproduction of intricate biostructures mimicking soft tissues, including cartilage and meniscus formations. These capabilities enhance preoperative planning applications and surgical outcomes through improved precision and reduced operative duration.

Commercial bioprinters are costly, and professional-grade 3D bioprinters costs may exceed $500,000 [38], presenting a significant barrier amid global healthcare budget constraints. Our conversion methodology, with initial costs ranging from $400-$500, offers a cost-effective alternative through the integration of open-source software and entry-level bioprinting hardware. This economic approach enables research facilities and healthcare providers to establish multiple bioprinting stations, facilitating efficient, scalable production of implants. The system's efficacy will be evaluated through prospective randomized trials, with particular focus on applications in pediatric orthopedics and traumatology.

Extrusion-based bioprinting demonstrates distinct advantages over alternative technologies through its capacity to process highly viscous biomaterials while minimizing cellular damage. Precise Z-offset control ensures optimal bioink deposition and prevents material spreading. Although dimensional variations in line width and joint thickness were observed due to bioink dispersion, several key relationships were identified: both low and high viscosity bioinks exhibited disrupted line formation when extruded through narrow apertures. The incorporation of collagen content in bioink formulations generated a fibrillar network that enhanced structural integrity, stabilized printed constructs, and minimized post-deposition material dispersion. This methodology proves particularly effective for fabricating biological structures, including monolayer soft and hard tissues, using viscous bioinks [39, 40]. Through decision tree analysis of printing outcomes, evaluating line width deviation, joint thickness, and printing continuity, Bioink D demonstrated superior performance characteristics.

A number of limitations were identified in both the printed materials and current bioprinter configuration. Air bubble formation in printed constructs, resulting from pressure differentials in the piping system, represents a significant challenge when working with liquid chemical mixtures. To mitigate pressure drops associated with variations in pipe diameter, flexible tubing was implemented for material transfer from reservoir to extruder. The peristaltic pump system was selected to address these challenges, providing continuous and consistent fluid flow through controlled compression and release mechanisms [41]. This design employs flexible tubes compressed by rollers or shoes, ensuring smooth material flow through positive compression. The system's enclosed nature, where liquid remains isolated from pump components, minimizes air introduction and subsequent bubble formation.

Cell damage in extrusion-based bioprinting is critically influenced by shear stress levels. Although cells exhibit considerable deformability and the ability to recover from mechanical strain, excessive shear stress can still lead to membrane and cytoskeleton damage, leading to cell death

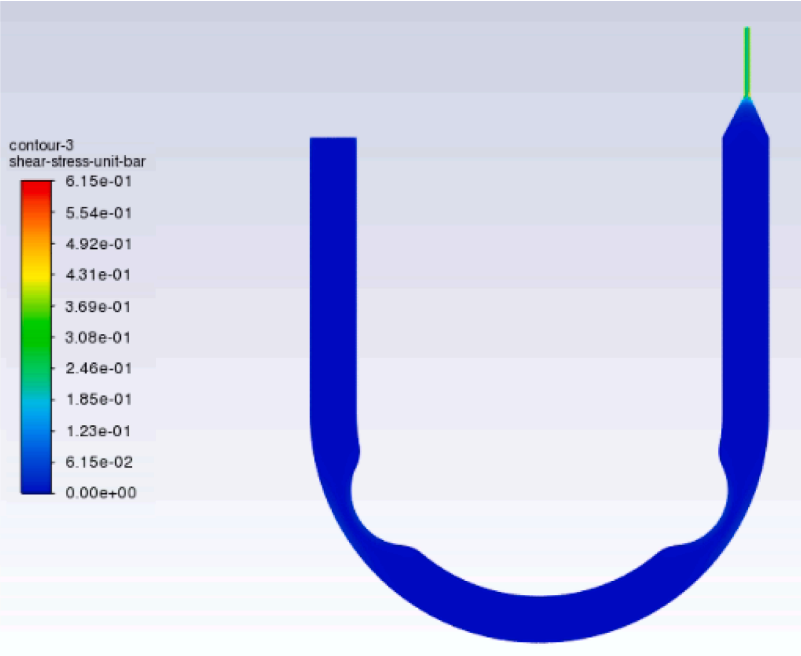

Fig. 12. 2D shear stress contour plot for bioink D though the tube and needle.

[32,33]. Factors including nozzle (needle) diameter and length [42] and flow-rate [29] are known to modulate the mechanical stress experienced by cells during extrusion. In this work, our experimental setup maintained a low flow rate and employed a nozzle with dimensions considered safe for cell's integrity. While elevated pressures in the range of 3–6 bar have been shown to significantly compromise viability by disrupting cell membranes, chondrocytes are relatively resilient and can sustain high viability rates under such conditions [43]. Previous studies have reported cell viability is almost 100 % from 0.05 to 0.10 bar shear stress [21] and it ranges from 60 % to 100 % at pressures up to 5 bar, depending on the applied hydrostatic load or extrusion parameters [42, 44]. Paxton et al. confirmed 100 % cell viability at 1 bar stress [44]. However, our modified bioprinter operated at a maximum extrusion pressure of 0.009 to 0.06 bar shear stress in the tube and approximately 0.45 bar, a level well within the safety threshold for a broad range of cell types. However, we acknowledge that direct cellular testing would strengthen our validation. While our system demonstrates mechanical compatibility with cell-appropriate bioinks, direct cellular viability testing represents an important next step in validating the system for tissue engineering applications.

In conclusion, we have successfully demonstrated the development of a cost-effective 3D bioprinting system optimized for hydrogel-based biomaterial fabrication. The system's heat-free extrusion mechanism makes it particularly suitable for printing cell-laden biomaterials, eliminating the risk of thermal-induced cell death during the fabrication process. Future research directions should focus on optimizing bioink formulations to achieve precise control over optical, mechanical, and dimensional properties, enabling the production of advanced biomaterials with enhanced functionality.

CRediT authorship contribution statement

Y. H. Dang: Hardware – control, coding, validation, Writing – original draft. **Elise Dauzat:** Methodology, Hardware – assembly, testing, and Bioink preparation, Writing – original draft. **Asif Istiak:** Hardware – assembly and testing, Printing and Sample evaluation. Rheological analysis, CFD simulation, Writing – review and editing draft. **Victoria Songe:** Methodology, Hardware – assembly, testing, and Bioink preparation, Writing – original draft. **Luke West:** Hardware – design and fabrication, assembly, Writing – original draft. **Kevin Jackson:** Hardware – design and fabrication, assembly, testing, Writing – original draft. **Md Imrul Kayes:** CAD drawing and simulation. **Md Saiful Islam:** Simulation result postprocessing. **Tanvir Faisal:** Conceptualization, Supervision, Writing – review & editing draft.

Funding

The authors acknowledge the financial support from Advance Course Improvement Grant (University of Louisiana at Lafayette).

Declaration of competing interest

The authors declare that they have no known competing financial interests or personal relationships that could have appeared to influence the work reported in this paper.

Supplementary materials

Supplementary material associated with this article can be found, in the online version, at doi:10.1016/j.stlm.2025.100212.

References

[1] Zhang B, et al. Highly stretchable hydrogels for UV curing based high-resolution multimaterial 3D printing. J Mater Chem B 2018;6(20):3246–53.
[2] Huang TQ, et al. 3D printing of biomimetic microstructures for cancer cell migration. Biomed Microdevices 2014;16:127–32.
[3] Zhang H-B, et al. Three-dimensional bioprinting is not only about cell-laden structures. Chin J Traumatol 2016;19(04):187–92.
[4] T Z, Hu HZ, Yin RX, Lu YD, Zhang WJ. Fabrication of three-dimensional organic/inorganic scaffold by direct ink writing technology. Beijing, China: ICAM-BM; 2018. p. 83–4.
[5] Tony A, et al. The additive manufacturing approach to polydimethylsiloxane (PDMS) microfluidic devices: review and future directions. Polymers (Basel) 2023;15(8):1926.
[6] Wang J, et al. Self-supporting electrodes for gas-involved key energy reactions. Adv Funct Mater 2021;31(43):2104620.
[7] Olakanmi EO, Cochrane RF, Dalgarno KW. A review on selective laser sintering/melting (SLS/SLM) of aluminium alloy powders: processing, microstructure, and properties. Prog Mater Sci 2015;74:401–77.
[8] Allum J, et al. Extra-wide deposition in extrusion additive manufacturing: a new convention for improved interlayer mechanical performance. Addit Manuf 2023;61:103334.

[9] Khamvongsa M, et al. Mechanical characterization of low-cost 3D FDM printed scaffolds fabricated with synthesized PLA/HA bio-composite filament. Ann 3D Printed Med 2025:100194.
[10] Istiak A, Hwang HY. Development of shape-memory polymer fiber reinforced epoxy composites for debondable adhesives. Mater Today Commun 2024;38.
[11] Quan H, et al. Photo-curing 3D printing technique and its challenges. Bioact mater 2020;5(1):110–5.
[12] Awad A, et al. 3D printing: principles and pharmaceutical applications of selective laser sintering. Int J Pharm 2020;586:119594.
[13] Ioannidis K, et al. A custom ultra-low-cost 3D bioprinter supports cell growth and differentiation. Front Bioeng Biotechnol 2020;8:580889.
[14] Salimi S, et al. Composite polyurethane adhesives that debond-on-demand by hysteresis heating in an oscillating magnetic field. Eur Polym J 2019;121:109264.
[15] Mirdamadi E, et al. FRESH 3D bioprinting a full-size model of the human heart. ACS Biomater Sci Eng 2020;6(11):6453–9.
[16] Tashman JW, Shiwarski DJ, Feinberg AW. A high performance open-source syringe extruder optimized for extrusion and retraction during FRESH 3D bioprinting. HardwareX 2021;9:e00170.
[17] Tashman JW, Shiwarski DJ, Feinberg AW. Development of a high-performance open-source 3D bioprinter. Sci Rep 2022;12(1):22652.
[18] Ji Z, et al. Facile photo and thermal two-stage curing for high-performance 3D printing of poly (Dimethylsiloxane). Macromol Rapid Commun 2020;41(10): 2000064.
[19] Rocca M, et al. Embedded multimaterial extrusion bioprinting. SLAS Technol: Transl Life Sci Innov 2018;23(2):154–63.
[20] O'Bryan CS, et al. Self-assembled micro-organogels for 3D printing silicone structures. Sci Adv 2017;3(5):e1602800.
[21] Blaeser A, et al. Controlling shear stress in 3D bioprinting is a key factor to balance printing resolution and stem cell integrity. Adv Heal Mater 2016;5(3):326–33.
[22] Lovecchio J, et al. Fiber thickness and porosity control in a biopolymer scaffold 3D printed through a converted commercial FDM device. Materials (Basel) 2022;15 (7):2394.
[23] Bessler N, et al. Nydus One Syringe Extruder (NOSE): a Prusa i3 3D printer conversion for bioprinting applications utilizing the FRESH-method. HardwareX 2019;6:e00069.
[24] Ozbolat IT, Chen H, Yu Y. Development of 'multi-arm bioprinter'for hybrid biofabrication of tissue engineering constructs. Robot Comput Integr Manuf 2014; 30(3):295–304.
[25] Wijnen B, et al. Open-source syringe pump library. PloS One 2014;9(9):e107216.
[26] Kyle S, et al. Printability'of candidate biomaterials for extrusion based 3D printing: state-of-the-art. Adv Heal Mater 2017;6(16):1700264.
[27] Yan Y, et al. Layered manufacturing of tissue engineering scaffolds via multi-nozzle deposition. Mater Lett 2003;57(18):2623–8.
[28] Nair K, et al. Characterization of cell viability during bioprinting processes. Biotechnol J: Healthc Nutr Technol 2009;4(8):1168–77.
[29] Li M, et al. Modeling mechanical cell damage in the bioprinting process employing a conical needle. J Mech Med Biol 2015;15(05):1550073.
[30] Müller M, et al. Alginate sulfate–nanocellulose bioinks for cartilage bioprinting applications. Ann Biomed Eng 2017;45:210–23.
[31] Rutz AL, Lewis PL, Shah RN. Toward next-generation bioinks: tuning material properties pre-and post-printing to optimize cell viability. MRS Bull 2017;42(8): 563–70.
[32] Boularaoui S, et al. An overview of extrusion-based bioprinting with a focus on induced shear stress and its effect on cell viability. Bioprinting 2020;20:e00093.
[33] Cidonio G, et al. The cell in the ink: improving biofabrication by printing stem cells for skeletal regenerative medicine. Biomaterials 2019;209:10–24.
[34] Liu Q, et al. Preparation and properties of 3D printed alginate–chitosan polyion complex hydrogels for tissue engineering. Polymers (Basel) 2018;10(6):664.
[35] GENDY ME, et al. Computational fluid dynamics simulation and visualization of Newtonian and non-newtonian transport in a peristaltic micro-pump. J Mech Med Biol 2021;21(08):2150058.
[36] Afjoul H, Shamloo A, Kamali A. Freeze-gelled alginate/gelatin scaffolds for wound healing applications: an in vitro, in vivo study. Mater Sci Eng: C 2020;113:110957.
[37] Saberian M, et al. How the combination of alginate and chitosan can fabricate a hydrogel with favorable properties for wound healing. Heliyon 2024;10(11).
[38] Osti F, et al. CT conversion workflow for intraoperative usage of bony models: from DICOM data to 3D printed models. Appl Sci 2019;9(4):708.
[39] Marques C, et al. Collagen-based bioinks for hard tissue engineering applications: a comprehensive review. J Mater Sci: Mater Med 2019;30:1–12.
[40] Stepanovska J, et al. Collagen bioinks for bioprinting: a systematic review of hydrogel properties, bioprinting parameters, protocols, and bioprinted structure characteristics. Biomedicines 2021;9(9):1137.
[41] Klespitz J, Kovács L. Peristaltic pumps—A review on working and control possibilities. In: 2014 IEEE 12th International symposium on applied machine intelligence and informatics (SAMI). IEEE; 2014.
[42] Li M, et al. Modeling process-induced cell damage in the biodispensing process. Tissue Eng C: Methods 2010;16(3):533–42.
[43] Wu Y, et al. Three-dimensional bioprinting of articular cartilage: a systematic review. Cartilage 2021;12(1):76–92.
[44] Paxton N, et al. Proposal to assess printability of bioinks for extrusion-based bioprinting and evaluation of rheological properties governing bioprintability. Biofabrication 2017;9(4):044107.